Electronic Supplementary Material

S-Enriched porous polymer derived N-doped porous carbons for electrochemical energy storage and conversion

Chao Zhang[1], Chenbao Lu[1], Shuai Bi[1], Yang Hou (✉)[3], Fan Zhang (✉)[1], Ming Cai[1], Yafei He[1], Silvia Paasch (✉)[4], Xinliang Feng[2,4], Eike Brunner[4], Xiaodong Zhuang[1]

1 State Key Laboratory of Metal Matrix Composites & Shanghai Key Lab of Electrical Insulation and Thermal Ageing, School of Chemistry and Chemical Engineering, Shanghai Jiao Tong University, Shanghai 200240, China

2 Chair for Molecular Functional Materials, Department of Chemistry and Food Chemistry, School of Science, Technische Universität Dresden, Mommensenstr. 4, 01069 Dresden, Germany

3 Key Laboratory of Biomass Chemical Engineering of Ministry of Education, College of Chemical and Biological Engineering, Zhejiang University, 310027 Hangzhou, China

4 Center for Advancing Electronics Dresden (cfaed), Technische Universität Dresden, 01062 Dresden, Germany

© Higher Education Press and Springer-Verlag GmbH Germany, part of Springer Nature 2018

E-mails: yhou@zju.edu.cn (Hou Y); fan-zhang@sjtu.edu.cn (Zhang F); Silvia.Paasch@tu-dresden.de (Paasch S)

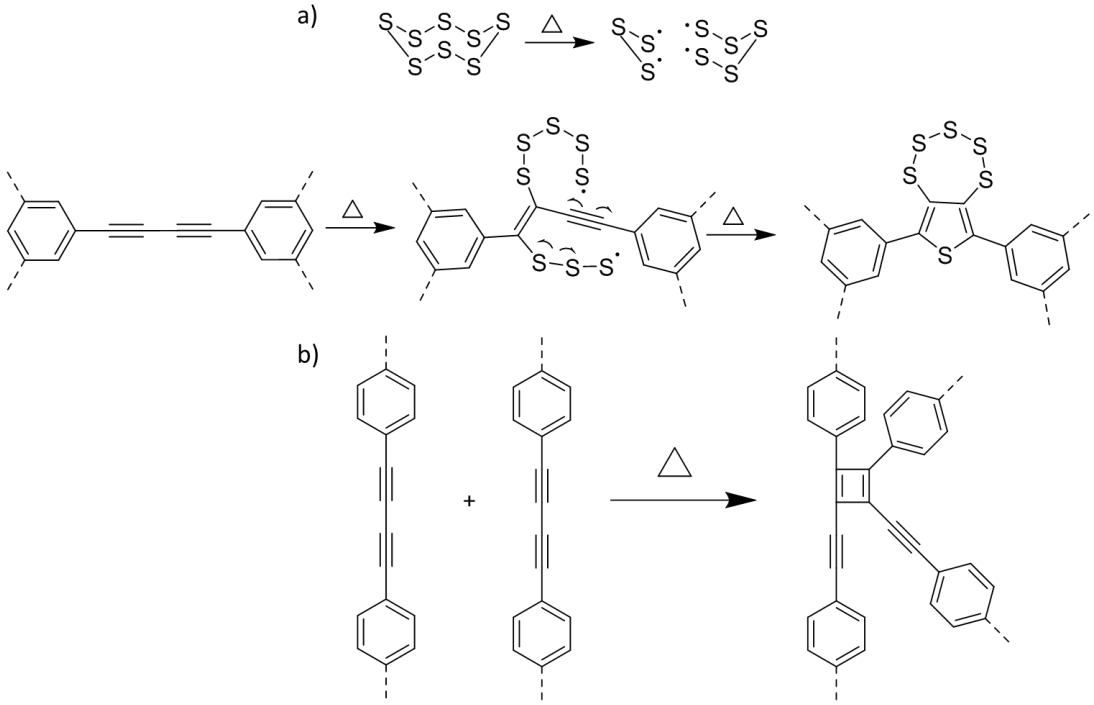

Fig. S1 a) Proposed mechanism.for the vulcanization process of PP-S [1]; b) proposed mechanism of formation of cyclobuta-1,3-diene

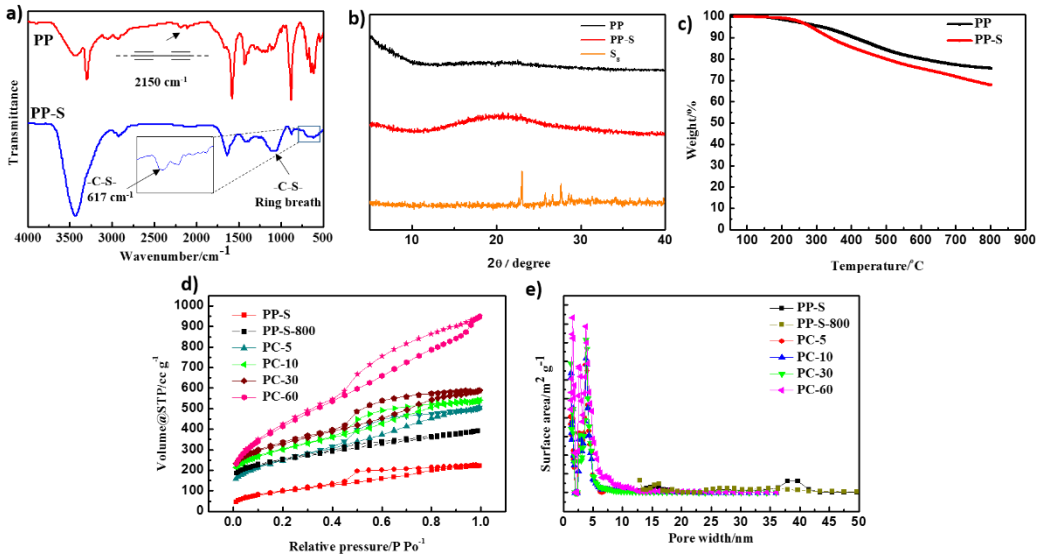

Fig. S2. a) FTIR spectra of PP and PP-S; b) PXRD patterns of PP, PP-S and S_8; c) TGA analysis of PP and PP-S under N_2 atmosphere at a heating rate of 10 ℃·min^{-1}; d) Nitrogen adsorption desorption isotherms and e) the pore size distribution of PP-S, PP-S-800 and PC-t

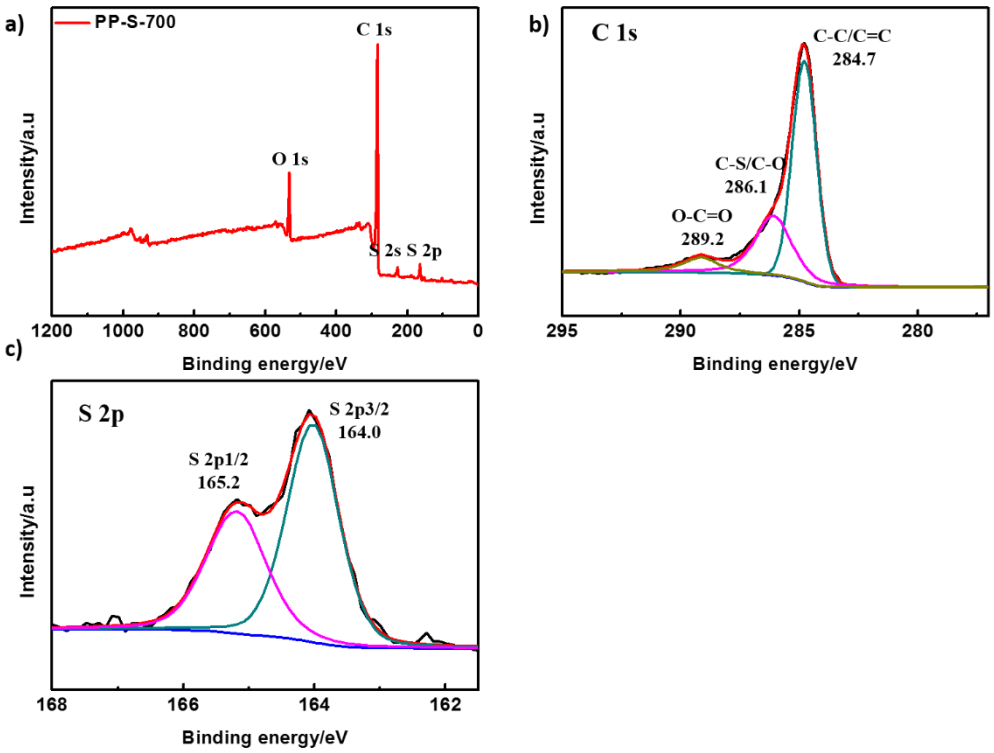

Fig. S3 a) Survey, b) C1s, c) S2p core level XPS spectra of the PP-S-700. PP-S-700 was prepared from PP-S being pyrolyzed under N_2 atmosphere at 700 ℃ for 1 h

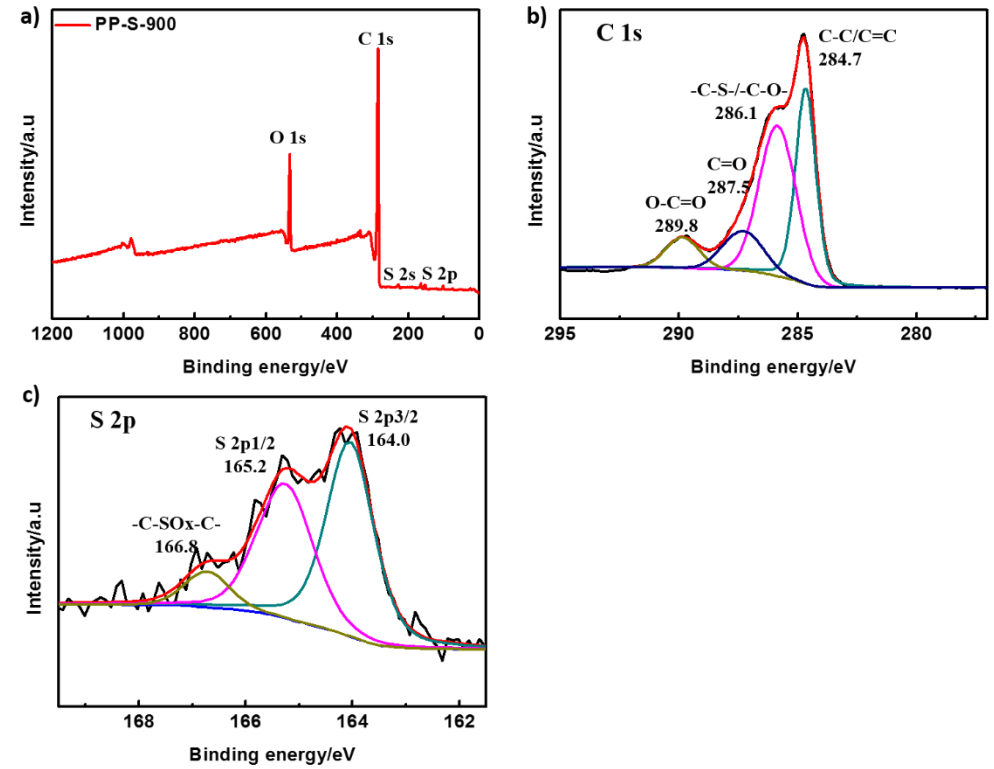

Fig. S4 a) Survey, b) C1s, c) S2p core level XPS spectra of the PP-S-900. PP-S-900 was prepared from PP-S being pyrolyzed under N_2 atmosphere at 900 ℃ for 1 h

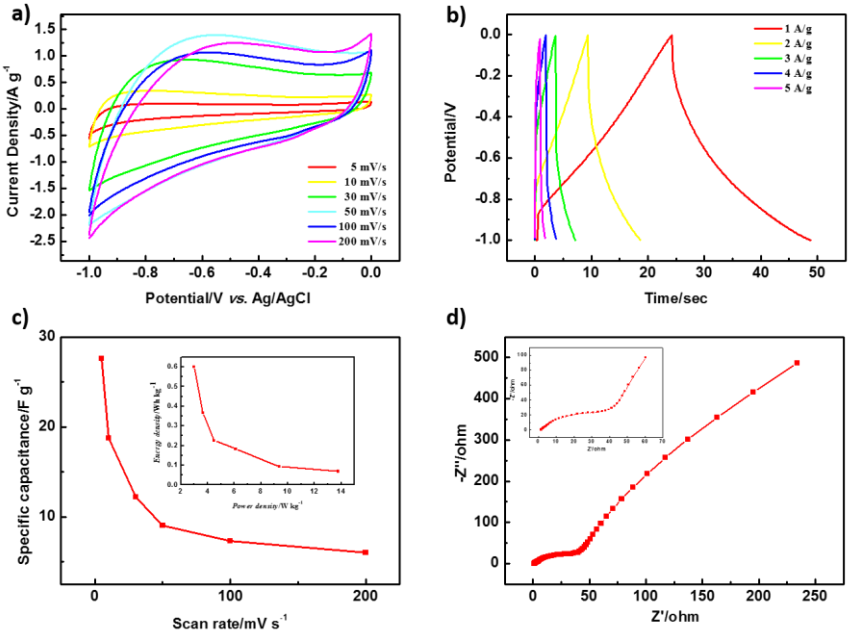

Fig. S5 Supercapacitor performance of PP-S. a) Cyclic voltammograms of PP-S at different scan rates; b) galvanostatic charge–discharge curves of PP-S at different current densities, respectively; c) specific capacitance plots at different scan rates for PP-S, the inset is Ragone plot of the supercapacitor; d) electrochemical impedance spectroscopy (EIS) profiles of PP-S measured in the frequency range from 0.01 Hz to 100 kHz (the inset shows the expanded high-frequency region of the plot)

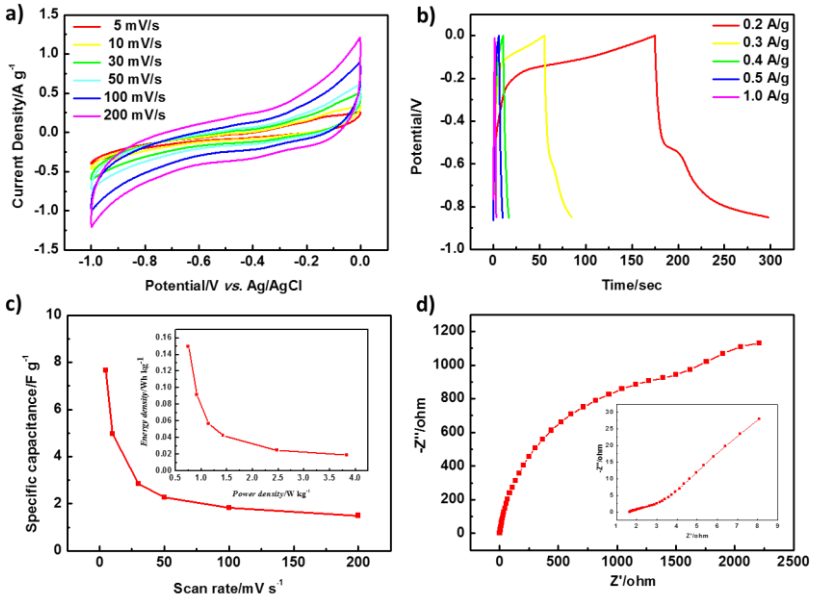

Fig. S6 Supercapacitor performance of PP-S-700. a) Cyclic voltammograms of PP-S-700 at different scan rates; b) galvanostatic charge–discharge curves of PP-S-700 at different current densities, respectively; c) specific capacitance plots at different scan rates for PP-S-700, the inset is Ragone plot of the supercapacitor; d) electrochemical impedance spectroscopy (EIS) profiles of PP-S-700 measured in the frequency range from 0.01 Hz to 100 kHz (the inset shows the expanded high-frequency region of the plot)

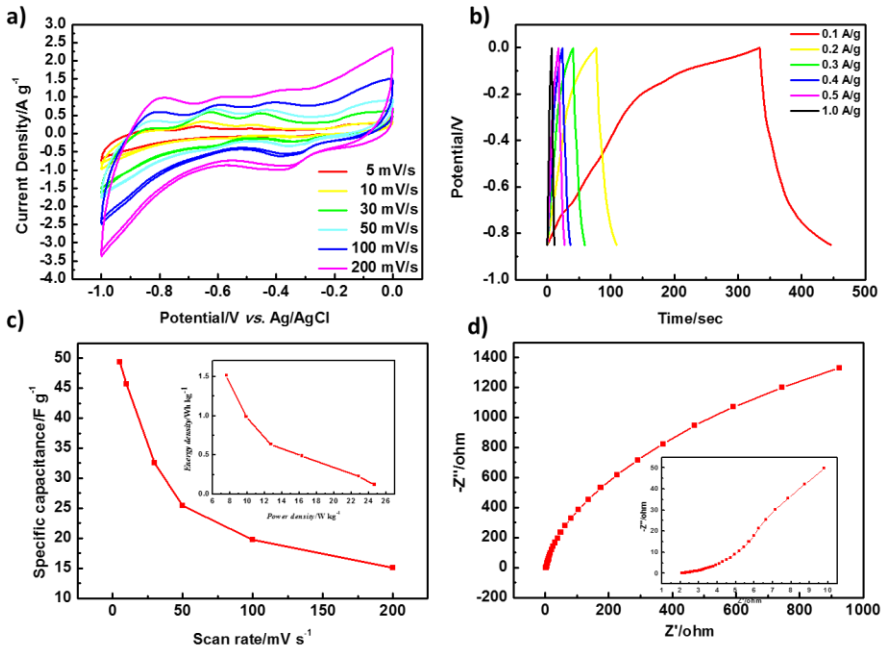

Fig. S7 Supercapacitor performance of PP-S-900. a) Cyclic voltammograms of PP-S-900 at different scan rates; b) galvanostatic charge–discharge curves of PP-S-900 at different current densities, respectively; c) specific capacitance plots at different scan rates for PP-S-900, the inset is Ragone plot of the supercapacitor; d) electrochemical impedance spectroscopy (EIS) profiles of PP-S-900 measured in the frequency range from 0.01 Hz to 100 kHz (the inset shows the expanded high-frequency region of the plot)

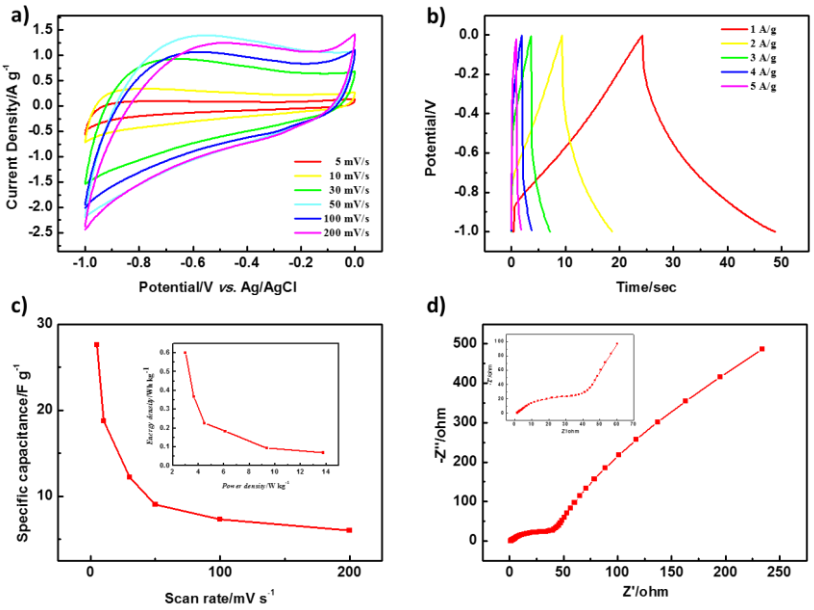

Fig. S8 Supercapacitor performance of PC-5. a) Cyclic voltammograms of PC-5 at different scan rates; b) galvanostatic charge–discharge curves of PC-5 at different current densities, respectively; c) specific capacitance plots at different scan rates for PC-5, the inset is Ragone plot of the supercapacitor; d) electrochemical impedance spectroscopy (EIS) profiles of PC-5 measured in the frequency range from 0.01 Hz to 100 kHz (the inset shows the expanded high-frequency region of the plot)

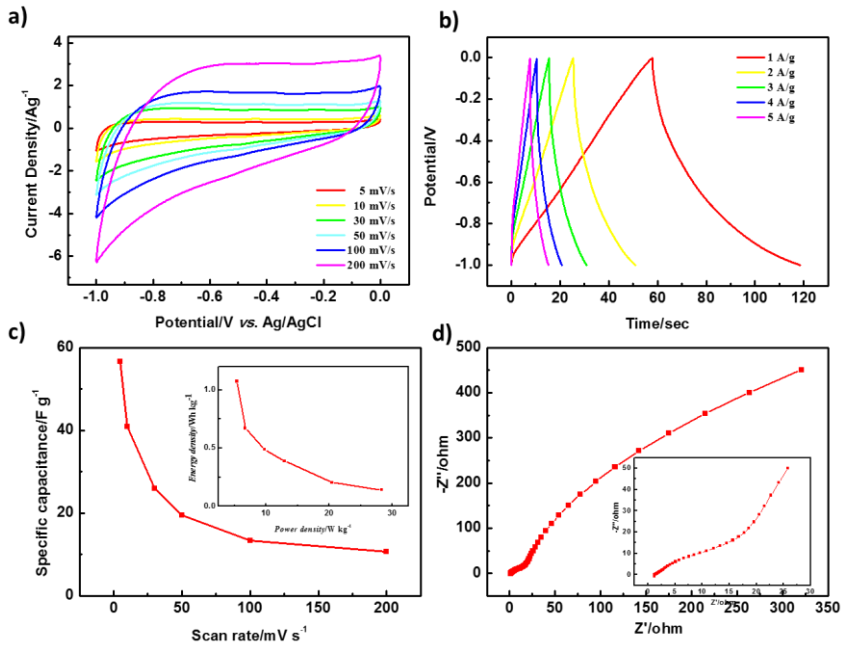

Fig. S9 Supercapacitor performance of PC-10. a) Cyclic voltammograms of PC-10 at different scan rates; b) galvanostatic charge-discharge curves of PC-10 at different current densities, respectively; c) specific capacitance plots at different scan rates for PC-10, the inset is Ragone plot of the supercapacitor; d) electrochemical impedance spectroscopy (EIS) profiles of PC-10 measured in the frequency range from 0.01 Hz to 100 kHz (the inset shows the expanded high-frequency region of the plot)

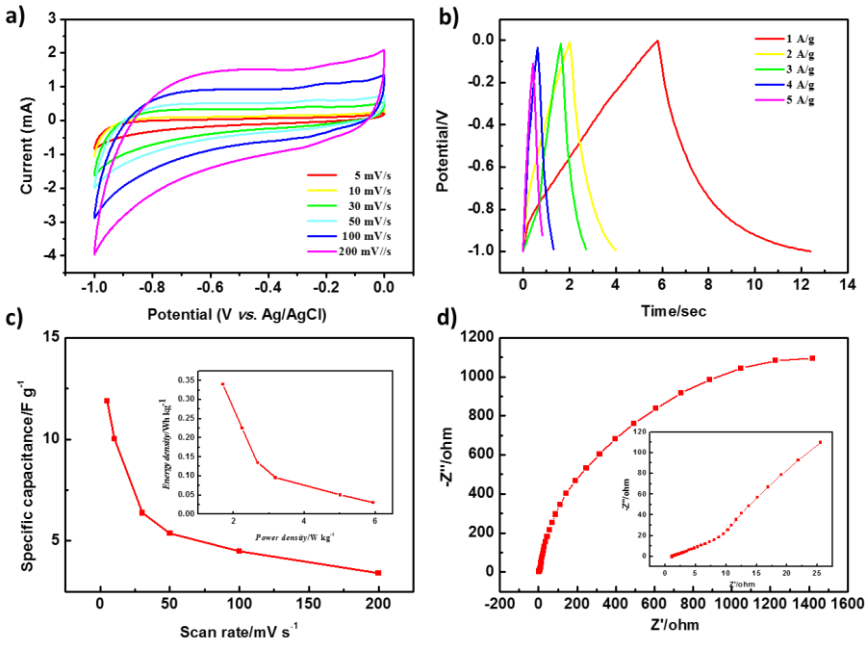

Fig. S10 Supercapacitor performance of PC-30. a) Cyclic voltammograms of PC-30 at different scan rates; b) galvanostatic charge–discharge curves of PC-30 at different current densities, respectively; c) specific capacitance plots at different scan rates for PC-30, the inset is Ragone plot of the supercapacitor; d) electrochemical impedance spectroscopy (EIS) profiles of PC-30 measured in the frequency range from 0.01 Hz to 100 kHz (the inset shows the expanded high-frequency region of the plot)

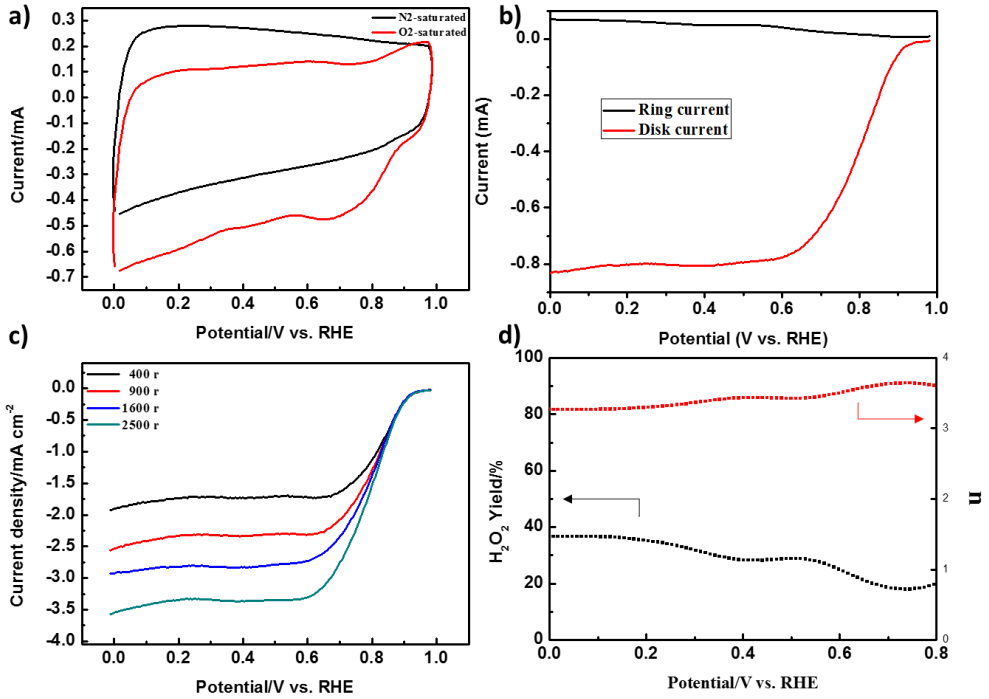

Fig. S11 (a) Cyclic voltammograms of the PC-5 in O_2- and N_2-saturated 0.1 mol·L^{-1} KOH solutions at a scan rate of 100 mV·s^{-1}; (b) rotating ring-disk electrode linear sweep voltammogram of PC-5 at a rotation rate of 1600 rpm; (c) RDE voltammograms recorded for the PC-5 in an O_2-saturated 0.1 mol·L^{-1} KOH solution at a scan rate of 10 mV·s^{-1} at different rotation rates (d) hydrogen peroxide concentration and electron transfer numbers of PC-5

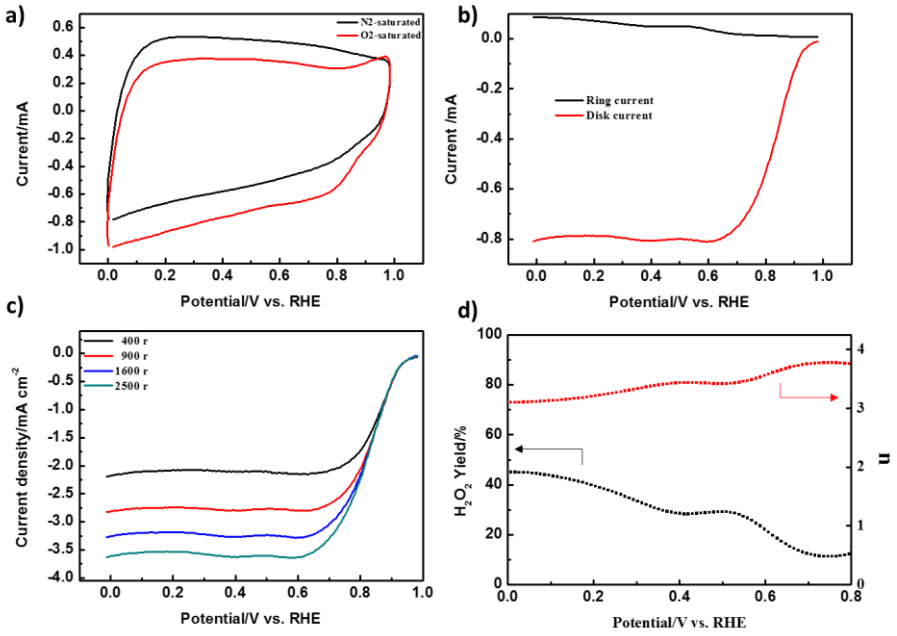

Fig. S12 (a) Cyclic voltammograms of the PC-10 in O_2- and N_2-saturated 0.1 mol·L^{-1} KOH solutions at a scan rate of 100 mV·s^{-1}; (b) rotating ring-disk electrode linear sweep voltammogram of PC-10 at a rotation rate of 1600 rpm; (c) RDE voltammograms recorded for the PC-10 in an O_2-saturated 0.1 mol·L^{-1} KOH solution at a scan rate of 10 mV·s^{-1} at different rotation rates (d) hydrogen peroxide concentration and electron transfer numbers of PC-10

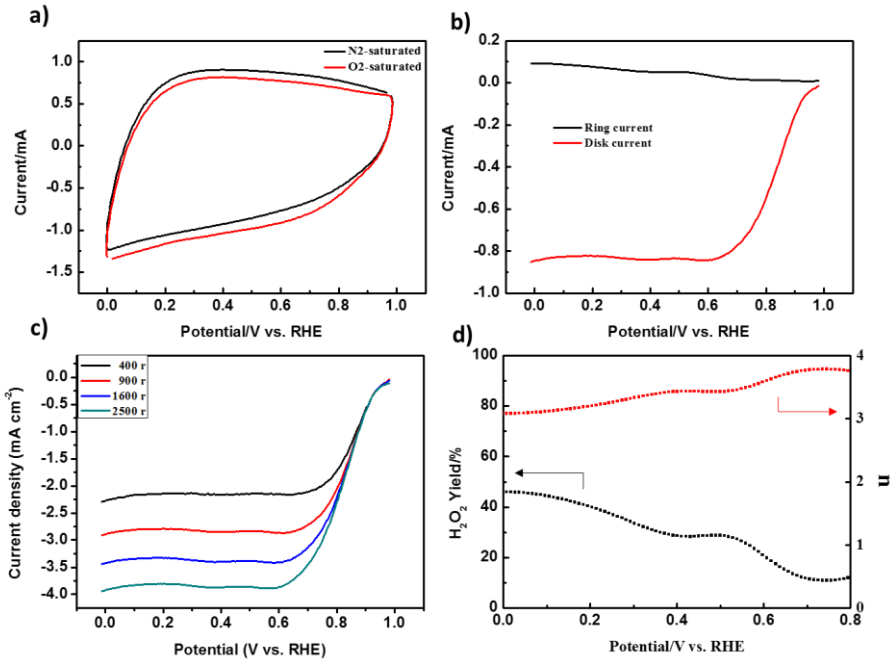

Fig. S13 (a) Cyclic voltammograms of the PC-30 in O_2- and N_2-saturated 0.1 mol·L^{-1} KOH solutions at a scan rate of 100 mV·s^{-1}; (b) rotating ring-disk electrode linear sweep voltammogram of PC-30 at a rotation rate of 1600 rpm; (c) RDE voltammograms recorded for the PC-30 in an O_2-saturated 0.1 mol·L^{-1} KOH solution at a scan rate of 10 mV·s^{-1} at different rotation rates (d) hydrogen peroxide concentration and electron transfer numbers of PC-30

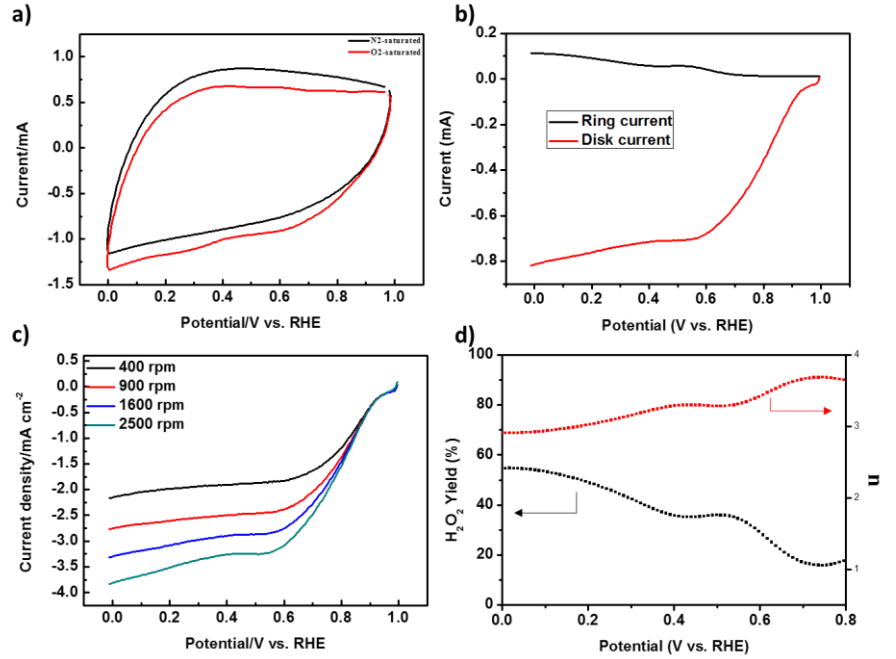

Fig. S14 (a) Cyclic voltammograms of the PC-60 in O_2- and N_2-saturated 0.1 mol·L^{-1} KOH solutions at a scan rate of 100 mV·s^{-1}; (b) rotating ring-disk electrode linear sweep voltammogram of PC-60 at a rotation rate of 1600 rpm; (c) RDE voltammograms recorded for the PC-60 in an O_2-saturated 0.1 mol·L^{-1} KOH solution at a scan rate of 10 mV·s^{-1} at different rotation rates (d) hydrogen peroxide concentration and electron transfer numbers of PC-60

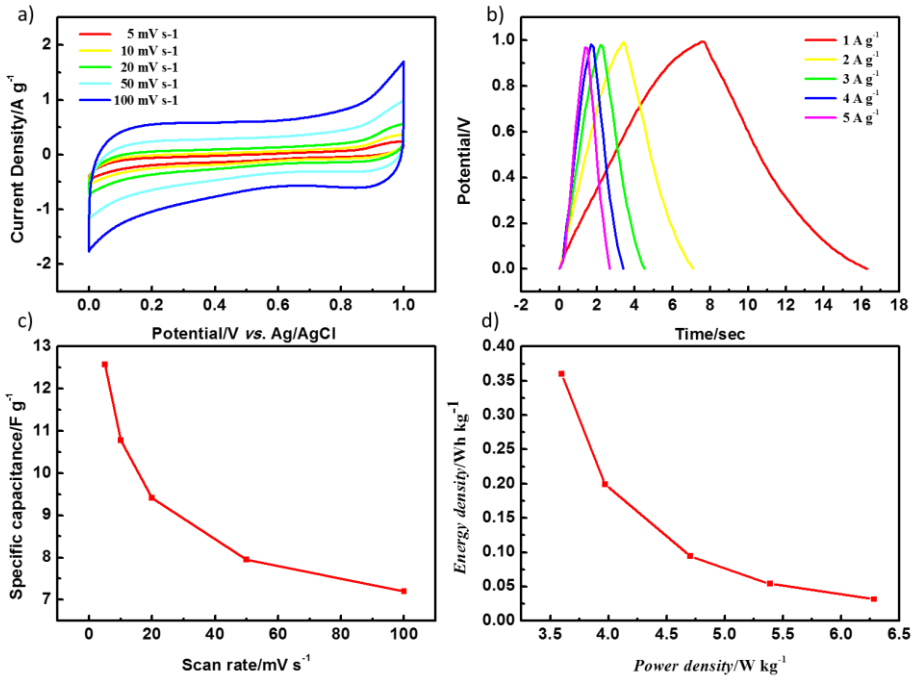

Fig. S15 Supercapacitor performance of PC-60 in the potential of 0-1 V. a) Cyclic voltammograms of PC-60 at different scan rates; b) galvanostatic charge–discharge curves of PC-30 at different current densities, respectively; c) specific capacitance plots at different scan rates for PC-60; d) ragone plot of the supercapacitor

Table S1 Elemental analysis PP-S and derived PC-t based on XPS

% mass Conc / Element / Sample	C	S	N
PP-S	63.7	36.3	0
PC-5	97.78	0.54	1.31
PC-10	98.18	0.50	1.32
PC-30	99.24	0.11	0.65
PC-60	99.50	0.05	0.45

Table S2 Relative content of different types of nitrogen of PC-t based on XPS

Relative content / N type / Sample	Quaternary N	Pyrrolic N	Pyridine N
PC-5	0.337	0.327	0.336
PC-10	0.334	0.333	0.333
PC-30	0.331	0.335	0.334
PC-60	0.331	0.337	0.332

Table S3 The selected typical reported supercapacitors based on porous carbons

Electrode material	Electrolyte	Specific capacitance	Cycling performance	Reference
N-doped GO	6.0 mol·L^{-1} KOH	424 F·g^{-1} (0.1 A·g^{-1})	/	[2]
N-doped rGO	6.0 mol·L^{-1} KOH	225 F·g^{-1} (0.5 A·g^{-1})	93% (1000 cycles)	[3]
P/N doped carbon	6.0 mol·L^{-1} KOH	236 F·g^{-1} (5 mV·s^{-1})	86% (5000 cycles)	[4]
CNFs@polypyrrole	6.0 mol·L^{-1} KOH	202 F·g^{-1} (1 A·g^{-1})	97% (3000 cycles)	[5]
N-enriched carbon from melamine-mica	6.0 mol·L^{-1} KOH	198 F·g^{-1} (1 A·g^{-1})	/	[6]
ZIF-derived porous Carbon-ZS	6.0 mol·L^{-1} KOH	285.8 F·g^{-1} (1 A·g^{-1})	97.8% (1000 cycles)	[7]
HPNC-NS	EMIMBF4	242 F·g^{-1} (0.1 A·g^{-1})	92% (10000 cycles)	[8]
Sulfur-doped porous rGO	/	343 F·g^{-1} (0.2 A·g^{-1})	96% (1000 cycles)	[9]
This work	6 mol·L^{-1} KOH	431.6 F·g^{-1} (5 mV·s^{-1})	99.74% (3000 cycles)	

References

[1] S. Debnath, A. Bedi, S.S. Zade, Thienopentathiepine: a sulfur containing fused heterocycle for conjugated systems and their electrochemical polymerization, Polym. Chem. 6(44) (2015) 7658-7665.

[2] X. Zhuang, F. Zhang, D. Wu, X. Feng, Graphene Coupled Schiff‐base Porous Polymers: Towards Nitrogen‐enriched Porous Carbon Nanosheets with Ultrahigh Electrochemical Capacity, Adv. Mater. 26(19) (2014) 3081-3086.

[3] Z. Lei, L. Lu, X. Zhao, The electrocapacitive properties of graphene oxide reduced by urea, Energy Environ. Sci. 5(4) (2012) 6391-6399.

[4] U.B. Nasini, V.G. Bairi, S.K. Ramasahayam, S.E. Bourdo, T. Viswanathan, A.U. Shaikh, Phosphorous and nitrogen dual heteroatom doped mesoporous carbon synthesized via microwave method for supercapacitor application, J. Power Sources 250 (2014) 257-265.

[5] L.F. Chen, X.D. Zhang, H.W. Liang, M. Kong, Q.F. Guan, P. Chen, et al., Synthesis of nitrogen-doped porous carbon nanofibers as an efficient electrode material for supercapacitors, ACS nano 6(8) (2012) 7092-7102.

[6] D. H. Jurcakova, M. Kodama, S. Shiraishi, H. Hatori, Z.H. Zhu, G.Q. Lu, Nitrogen-Enriched Nonporous Carbon Electrodes with Extraordinary Supercapacitance, Adv. Funct. Mater. 19(11) (2009) 1800-1809.

[7] S. Zhong, C. Zhan, D. Cao, Zeolitic imidazolate framework-derived nitrogen-doped porous carbons as high performance supercapacitor electrode materials, Carbon 85 (2015) 51-59.

[8] J. Hou, C. Cao, F. Idrees, X. Ma, Hierarchical porous nitrogen-doped carbon nanosheets derived from silk for ultrahigh-capacity battery anodes and supercapacitors, ACS nano 9(3) (2015) 2556-2564.

[9] X.A. Chen, X. Chen, X. Xu, Z. Yang, Z. Liu, L. Zhang, et al., Sulfur-doped porous reduced graphene oxide hollow nanosphere frameworks as metal-free electrocatalysts for oxygen reduction reaction and as supercapacitor electrode materials, Nanoscale 6(22) (2014) 13740-13747.